Type II radio bursts: 2. Application of the new analytic formalism

J. M. Schmidt[1] and Iver H. Cairns[1]

Received 10 May 2012; revised 12 September 2012; accepted 23 September 2012; published 8 November 2012.

[1] Type II radio bursts drift in frequency as shock waves and coronal mass ejections (CMEs) move through the Sun's corona and the solar wind. This paper applies an extended analytic theoretical model for type II radio bursts to an MHD simulation of the rippled shock front found upstream of the flanks of a CME. The theory treats the acceleration of electrons at the shock, formation of electron beams, growth of Langmuir waves, and conversion of Langmuir energy into radiation. The extended theory is entirely analytic and includes kappa electron velocity distribution functions for the ambient plasma electrons and the shock-reflected electrons. It also includes the plateauing of the electron beam, which releases energy for the Langmuir waves. This paper presents and discusses our numerical results for synthetic radio source regions and synthetic dynamic spectra, gained by applying our radiation model to an MHD simulation of a shock driven by a CME. The investigation reveals strong emission upstream of the flanks of the shock. A complicated rippled shock geometry develops with embedded "ripples" that stimulate short-lived "bright spot" radio sources, which lead to complicated substructures in the dynamic spectrum, and more extended sources that usually have a weaker and more diffuse radio emission. The natural development of ripples on the shock provides a natural link between the ripple theory of Knock, Cairns, and colleagues and the bolt-on model presented here.

Citation: Schmidt, J. M., and I. H. Cairns (2012), Type II radio bursts: 2. Application of the new analytic formalism, *J. Geophys. Res.*, *117*, A11104, doi:10.1029/2012JA017932.

1. Introduction

[2] Propagating shock waves in the solar corona and interplanetary medium have strong associations with type II solar radio emission [*Wild and Smerd*, 1972; *Cane et al.*, 1981; *Nelson and Melrose*, 1985; *Lengyel-Frey et al.*, 1997]. A close correlation between type IIs and the shocks ahead of coronal mass ejections (CMEs) has been found in recent interplanetary observations. These shocks are thought to be generated with a mechanical piston mechanism, yet very fast coronal shocks are also discussed as blast waves caused by the pressure pulse of a flare [see, e.g., *Temmer et al.*, 2009; *Nindos et al.*, 2011]. At least some type IIs show strong evidence of generation in electron foreshock regions upstream of the shock waves ahead of CMEs [*Cane et al.*, 1981; *Reiner et al.*, 1997, 1998; *Bale et al.*, 1999; *Reiner and Kaiser*, 1999; *Mann and Klassen*, 2005; *Pulupa et al.*, 2010; *Cairns*, 2011]. These papers provide observational demonstrations that (1) the emission is consistent with generation near the upstream electron plasma frequency f_p and near $2f_p$, whereby an association between interplanetary (hectometric and kilometric) type II bursts and CME-driven shocks is firmly established [*Cane et al.*, 1987; *Reiner at al.*, 1998], (2) the source region is traveling away from the Sun at a speed of hundreds of km s^{-1}, as indicated by plots of the inverse emission frequency versus time, consistent with a propagating shock, and (3) Langmuir waves and electron beams can occur in the foreshock region ahead of an active type II–emitting CME-driven shock.

[3] CMEs are major transient events carrying away mass and momentum from the corona of the Sun [e.g., *Hundhausen*, 1999], which are observed with coronagraphs and spacecraft in situ measurements. Measured speeds range between less than 100 and in excess of 3000 km/s, with masses as large as 10^{13} kg [*Hundhausen*, 1999; *St. Cyr et al.*, 2000; *Gopalswamy*, 2006]. When the CME is moving faster than the local fast mode speed it can drive a shock, which is capable of accelerating electrons that produce type II radio bursts. The typical formation region for type II radio bursts is from heliocentric distances $\geq 2\ R_\odot$ ($R_\odot$ is the solar radius) [e.g., *Gopalswamy et al.*, 2005]. Radio observations from within $\sim 4\ R_\odot$ heliocentric distance to near 1 AU have potential for predicting the precise behavior of CMEs for space weather applications [e.g., *Gopalswamy et al.*, 2000; *Cairns*, 2011].

[4] The accepted picture for type II emission involves four main steps [e.g., *Nelson and Melrose*, 1985; *Mann and Klassen*, 2005; *Cairns*, 2011]: (1) electrons are accelerated

[1]School of Physics, University of Sydney, Sydney, New South Wales, Australia.

Corresponding author: J. M. Schmidt, School of Physics, University of Sydney, Sydney, NSW 2006, Australia. (jschmidt@physics.usyd.edu.au)

0148-0227/12/2012JA017932

at or near the shock, (2) accelerated electrons form velocity space beam distributions in the foreshock region, (3) beam distributions are unstable to the generation of Langmuir waves via wave-particle interactions, and (4) Langmuir waves produce electromagnetic emission, leading to the observed type II burst. *Holman and Pesses* [1983], *Nelson and Melrose* [1985], *Cairns* [1986], and *Benz and Golla* [1988] have considered qualitative models for type II production in foreshock regions upstream of shocks before.

[5] The angle θ_{bn} between the upstream magnetic field direction and the local shock normal is an important quantity for deciding what electron acceleration process is relevant. Acceleration of reflected electrons at quasiperpendicular shocks ($|\theta_{bn}| \geq 45°$) is dominated by shock drift acceleration (SDA). This acceleration is also known as magnetic mirror reflection, and it produces large relative energy gains when $|\theta_{bn}| \sim 90°$. *Bale et al.*'s [1999] in situ observation of a shock associated with an interplanetary type II suggested magnetic connection of the spacecraft to two tangent points ($\theta_{bn} = 90°$) on opposite sides of the spacecraft prior to the shock crossing (with $\theta_{bn} \sim 86°$ at the crossing). This implies the existence of ripples of the shock surface [*Bale et al.*, 1999; *Knock et al.*, 2003b; *Neugebauer and Giacolone*, 2005; *Knock and Cairns*, 2005; *Pulupa et al.*, 2010], where parts of the shock magnetically connected to the upstream region do not have the same θ_{bn} as at the shock crossing. In the case that the shock is curved (even without ripples) or if **B** varies in space, the same is likely. One would expect multiple noncontiguous upstream regions magnetically connected to the shock with a large range of θ_{bn}, often with one or more points with $|\theta_{bn}| \sim 90°$ present, in such a case.

[6] *Knock et al.* [2003b] further discussed the influence of shock ripples on the dynamic spectra. These produce significant fine structures in time and frequency. The modeling of coronal and interplanetary structures was included by *Knock and Cairns* [2005]. A further improvement of the model was achieved by including a data-driven model for the solar wind with both radial and longitudinal (azimuthal) variations in plasma parameters, again leading to significant fine structures and variability of the dynamic spectrum [*Florens et al.*, 2007]. *Hillan et al.* [2012a, 2012b] carried out a first detailed comparison of the model with observations.

[7] *Schmidt and Gopalswamy* [2008] replaced the computing-intensive numerical evaluations of phase space integrals for the calculation of reflected beam parameters in the type II theory [*Knock et al.*, 2001, 2003a, 2003b; *Knock and Cairns*, 2005; *Cairns and Knock*, 2006; *Florens et al.*, 2007] with analytic results for the beam parameters for Maxwellian electron velocity distributions in the solar wind, and "bolted" the then completely analytical radiation theory onto an MHD simulation of a CME-driven shock. They were able to produce results similar to the radio map observations of *Maia et al.* [2000]. A number of limitations exist for that calculation [*Cairns*, 2011].

[8] In the first part of the first paper of this series [*Schmidt and Cairns*, 2012, hereinafter referred to as paper 1], we extended the *Schmidt and Gopalswamy* [2008] approach to treat kappa electron distribution functions in the solar wind, with elongated high-velocity tails, which better suit solar wind conditions [see, e.g., *Maksimovic et al.*, 1997]. Observations imply $\kappa \approx 2.5$ typically in the solar wind [e.g., *Maksimovic et al.*, 1997], which we use in our simulations. We also applied the kinetic radiation theory thoroughly in the upstream region of the shock so as to avoid unphysical production of radiation in the downstream region, and included analytically the so-called "quasilinear plateauing" effect on the reflected beam distribution, which results from erosion of the reflected distribution as Langmuir waves are generated. The theory developed in paper 1 involves several steps. We calculated exact results for the reflection efficiencies of a kappa distribution of electrons incident on a general shock, which are used to derive exact reflected electron beam distributions throughout the upstream region. Our analytic treatment of the quasi-linear plateauing effect caused by growth of Langmuir waves is then applied to the reflected electron beam distributions, and used to compute the reflected electron beam number density, velocity, and width in velocity space. The latter three parameters enter the radiation theory of *Robinson and Cairns* [1998a, 1998b] for the analytic calculation of volume emissivities of fundamental and harmonic plasma radiation. The specific nonlinear processes used are (1) the electrostatic decay $L \rightarrow L' + S$ of beam-driven Langmuir waves L, backscattered Langmuir waves L', and ion acoustic waves S, (2) the electromagnetic decay $L \rightarrow T(f_p) + S'$, stimulated by the S wave products of the electrostatic decay, to produce fundamental radiation T (f_p) and ion acoustic waves S', and (3) the coalescence $L + L' \rightarrow T(2f_p)$ to produce harmonic radio waves T ($2f_p$). We then used this new bolt-on theory to predict the radio emission produced upstream of the nose (most antisunward) region of a CME-driven shock. The shock was predicted using an MHD simulation code. We obtained a much more refined picture of shock radiation than in *Schmidt and Gopalswamy* [2008], which also complemented the predictions of *Knock et al.* [2003b], *Knock and Cairns* [2005], and *Hillan et al.* [2012a, 2012b] for example. In particular, we showed that the radio emission field excited at the nose of the shock was a crescent or sickle-like shape with the maximum emission slightly above the ecliptic plane. The reason for this asymmetry was a reconnection site at the northern edge of the CME, which shifted magnetic field lines and increased θ_{bn} in the Northern Hemisphere. The fading of the radio source toward the northern and southern edges of that moon crescent area was due to a decrease of the local beam velocity of the reflected electrons in those directions. The integrated radio fluxes of that radiation field yielded drifting spectra in good qualitative agreement with some observations. A fading of these drifting lines occurred when the CME decelerated.

[9] In the present paper we extend our study of shock-excited radio emission to focus on the flanks of the CME-driven shock, where ripples in the shock front develop [*Bale et al.*, 1999; *Knock et al.*, 2003b; *Pulupa et al.*, 2010; *Hillan et al.*, 2012a, 2012b] and lead to modulations of θ_{bn} with position on the shock. These ripples can lead to many locations where the shock is closely perpendicular with $\theta_{bn} \approx 90°$. These places excite strong reflected electron beams and torch-like radio sources that extend far from the shock surface. As the shock evolves, the ripples, shock properties, and radio emission vary with time. These evolving radio sources associated with bright spots on the shock front cause a complicated multiline structure of the resulting dynamic spectra. The present simulation predicts the dominant emission to come from the flanks of this macroscopic shock rather than the nose, due primarily to the quasi-radial

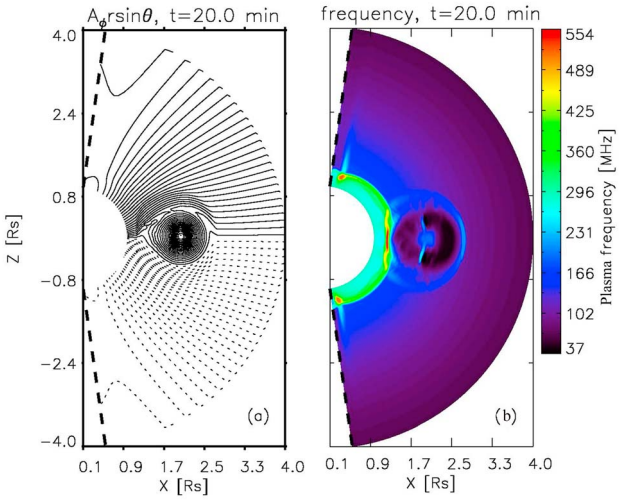

Figure 1. (a) Magnetic field line configuration in and around the CME at time t = 20 min after the launch of the CME. Solid and dashed lines show positive and negative values of the vector potential, yet in both cases the magnetic field lines are outward directed. (b) Distribution of f_p.

magnetic field structures in the simulation. The natural development of ripples on the shock provides a natural link between the "ripple" theory of *Knock et al.* [2003b], *Knock and Cairns* [2005], *Cairns and Knock* [2006], and *Hillan et al.* [2012a, 2012b], and our bolt-on model, which shows that ripples are often very important in producing type II emission.

2. MHD Model

[10] The MHD code used in this work is based on a flux-corrected transport (FCT) scheme for solving the MHD equations in spherical coordinates and in conservative form for the density ρ, velocity **v**, magnetic field **B**, and pressure p of a physical system, as described by *Zalesak* [1979] and *DeVore* [1991]. Rotational symmetry around the rotation axis $z = r\cos\theta$ of the Sun is assumed here; i.e., all fields are considered to be independent of the azimuthal coordinate ϕ. The in-ecliptic coordinate is $x = r\sin\theta$. Thus, the code is 2.5-dimensional [see, e.g., *Cargill et al.*, 2000, for further details]. The computational grid consists of 300 $\times$ 100 points in the $r - \theta$ plane, and only 5 cells in ϕ, in which the radial extension of the simulation box is from $R_\odot$ to 4 $R_\odot$ with the origin at the Sun's center. The boundary conditions are floating, except at the inner boundary, where initial quantities for the density ρ, velocity **v**, magnetic field **B** and the pressure p of a radial and adiabatical Parker solar wind are kept constant.

[11] Details of the MHD simulation setup, evolution, and plasma quantities are described in paper 1 and only a brief summary is provided here. A CME is introduced as a flux rope of cylindrical shape that extends like a torus around the z axis and is embedded in an appropriately distorted radial solar magnetic field. The initial internal pressure of the CME is increased by a factor of three with respect to the external solar wind pressure, according to measurements of overexpanding CMEs [e.g., *Gosling et al.*, 1998].

[12] Magnetic field line configurations in the r-θ plane are described by using contour plots of the quantity $A_\phi r\sin\theta$, where A_ϕ is the ϕ component of the vector potential, as illustrated in Figure 1a [*Schmidt and Cairns*, 2012]. The field line configuration is the combination of the flux rope's twisted magnetic field lines, which when projected into the x-z plane are nearly circular and have an counterclockwise sense of rotation, and a radial magnetic field originating from the solar surface and directed away from the Sun. Since the outer magnetic field has an opposite sense to the rope's magnetic field in the Northern Hemisphere, we find a point with exactly antiparallel and reconnecting magnetic field lines at the northern edge of the flux rope. This point clearly shows the characteristic "necking" shape of magnetic field lines at a x point reconnection region.

3. Identification of Flank Shocks

[13] In Figure 1b we display the spatial distribution of f_p (and so the plasma density) within and surrounding the CME eruption, 20 min after the launch of the CME, in a plane spanned by the in-ecliptic (x) axis and the Sun's rotation axis (z) for the same MHD simulation as in paper 1. The body of the CME can be discerned as the dark circle in the middle of the image. This is a rarefaction region, which develops when the CME overexpands due to internal overpressure. In the middle of the circular region is a blue region that corresponds to a small increase in the density centered around the centroid of the CME. The local maximum of the density is identical with the midpoint of the CME. We developed an automatic capturing routine for the midpoint of the CME that can identify this local maximum of the density field. This capturing routine can be applied to successive temporal cuts of the MHD simulation of the erupting CME and thus traces the midpoint of the CME.

[14] Figure 2 shows the configuration of a pointer, attached to the center of the CME, which is located at position (x_0, z_0), that scans a location on the shock front of the CME-driven shock. This pointer has a rotation angle α measured clockwise from the rotation axis z of the Sun. The shock front is indicated as the large oval in Figure 2. Thus values of α between about $-60°$ and $0°$ parameterize the northern flank of the CME-driven shock, and α values between about $180°$ and $240°$ parameterize the flank shock of the CME in the Southern Hemisphere. The domain $\alpha \in (0°, 180°)$ belongs to the nose region of the shock and was treated in paper 1. That domain can also be treated with the present paper's technique.

[15] We identify the three-dimensional location and characteristics of the CME-driven shock using the variations of the plasma density and velocity along multiple straight lines with different α from the CME midpoint. The shock front is characterized by a density pile-up originating from the initial push of the expanding CME, with a sharp decrease marking the shock ramp. We have developed an automated routine that can determine the spatial position of the local maximum of this density pile-up (and associated changes in plasma velocity, **B**, and temperature) along that ray. This routine also detects the spatial position of a kink in the density profile in the upstream region of the shock along the same

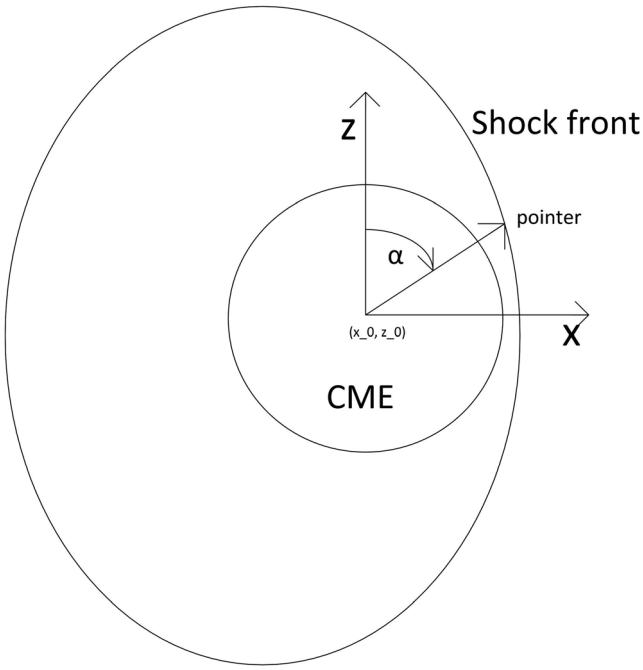

Figure 2. Rotation angle α, defined clockwise from the positive z axis, for a pointer centered on the CME's midpoint (x_0, z_0) that scans points on the CME-driven shock front.

ray. We define the position of the local maximum as the border point of the downstream region and the position of the kink position as the border point of the upstream region. The region between the local density maximum and the kink position is defined to be the shock ramp. Consistent with this, we find that the position of the entropy jump, which is another definition of the shock front, is usually between the density maximum and the kink.

[16] Figure 3 displays the profile of the number density n along the ray $\alpha = 0°$ at time $t = 20.0$ min after the launch of the CME. The quantity s is the coordinate along the ray, centered on the midpoint of the CME and measured in solar radii. Hence, a positive value of s corresponds to the Northern Hemisphere for this α, and a negative value of s corresponds to the Southern Hemisphere. For $s > 0$ we find a steep maximum of the number density of about 1.1×10^8 m^{-3} at about $s = 0.57\ R_\odot$. It is labeled max in the graph. At $s \approx 0.78\ R_\odot$ and $n_e \approx 4.5 \times 10^7$ m^{-3} we find the kink. We see in this example that there is a steep and strong shock ramp. We find a similar shock pattern in the negative s regime, this time with a smaller density jump.

[17] Figure 4 shows normalized profiles for other physical quantities along the same ray with $\alpha = 0°$ and $t = 20.0$ min. The speed profile (solid line), actually $|\mathbf{v}|/770$ km s^{-1}, has two kinks at the positions where the upstream regions start, identical with the "kink" positions in Figure 3. The dotted line shows the normalized magnetic field profile along the $\alpha = 0°$ ray. Again, we find two kinks at the same kink positions as in Figure 3. Finally, the normalized temperature profile (dashed line) has two kinks at the same locations as the kinks in $n(s)$. Although the profiles of Figure 4 are also well suited to determine the boundaries of the upstream

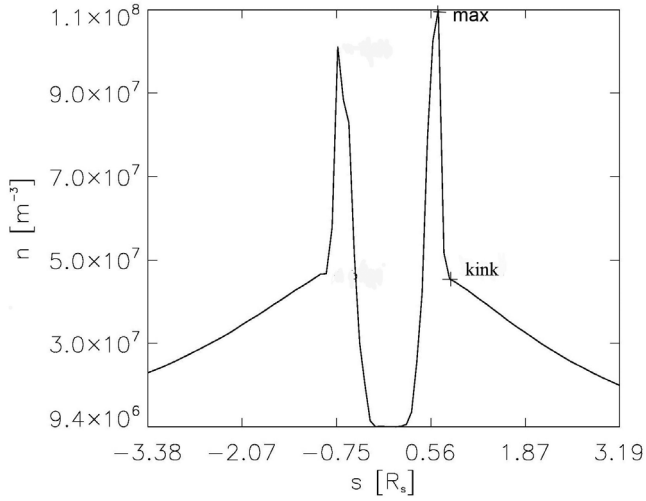

Figure 3. Number density profile at time $t = 20$ min along a ray ($\alpha = 0°$) from the center of the CME ($s = 0$) in the northward ($s > 0$) and southward ($s < 0$) directions. The shock is located at the strong and steep gradient between the maximum (max) and kink positions.

region of the shock, the number density profile in Figure 3 gives us a clearer picture of the ramp of the shock and thus is used in this paper to identify the positions where the upstream and downstream regions of the shock start.

[18] By varying α the three-dimensional location of the shock front can be obtained and the local shock properties determined. In addition, ripples and indentations in the shock front can be identified and characterized.

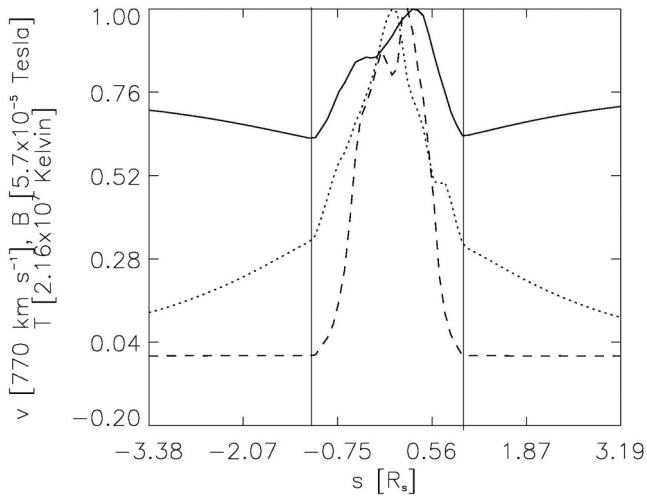

Figure 4. Normalized flow speed (solid line), magnetic field (dotted line), and temperature (dashed line) profiles at $t = 20$ min along the ray $\alpha = 0°$ from the center of the CME ($s = 0$) in the northward ($s > 0$) and southward ($s < 0$) directions. The vertical lines show that the kinks in the speed, magnetic field, and temperature profiles are at the same positions as the kink positions in the number density profile.

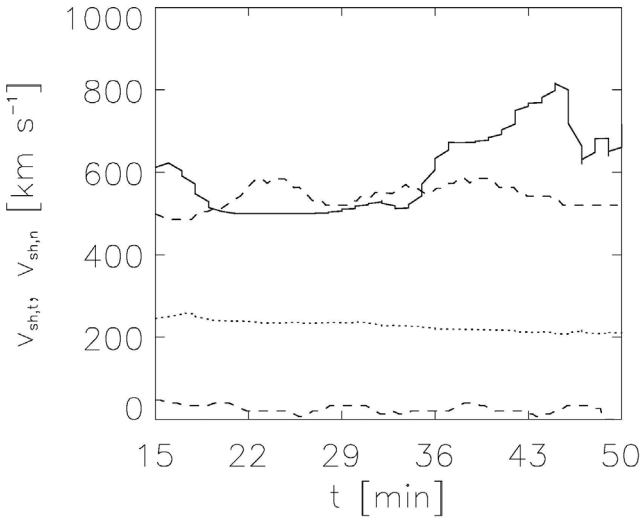

Figure 5. Normal speed $v_{sh,n}$ (dotted line) and tangential speed $v_{sh,t}$ (solid line) of the shock at $\alpha = 0°$ as functions of time in the solar wind frame. Note that $v_{sh,t}$ is much larger than $v_{sh,n}$, showing that the shock is moving like a ballistic object with a velocity primarily along the x axis. The top dashed line shows the radial speed of the CME core (v_x), and the bottom dashed line shows its lateral expansion speed (v_z) for comparison.

4. Calculation of Shock Properties

[19] Shock properties are now calculated for each ray using the Rankine-Hugoniot conditions and plasma parameters found at the upstream/downstream position. Note that although the Rankine-Hugoniot conditions are applicable only to a stationary 1-D flow, the shock evolution is rather slow, which means that it can be treated as a series of quasi-stationary states. In addition the shock surface, including curvature and ripples, is typically only weakly curved locally. Thus, the 1-D approximation is reasonable. The shock normal is approximated as the direction of the ray for each α. This is reasonable if an almost radially expanding CME drives the shock and the foot point of the α ray is close to the center point of the expansion. The upstream direction of the magnetic field with respect to this normal can be evaluated using the magnetic field values from the MHD simulation just upstream (three grid cells) of the position of the upstream kink, yielding θ_{bn}. Upstream and downstream values of density, solar wind velocity and magnetic field are then used to calculate the normal and tangential shock velocity with respect to the local shock normal (also compare with the formalism we developed in paper 1). On performing this procedure for many α and t, we find that the 3-D location of the shock is well defined, as described in more detail below. For regions on the flanks of the shock, the shock motion in the tangential direction follows closely the ballistic (radial) motion of the CME, yet there is only a moderate shock motion in the normal (almost radial) direction. This corresponds to the CME moving primarily ballistically along the $x = 0$ axis, with only a relatively slow expansion transverse.

[20] Figure 5 shows the speeds $v_{sh,t}$ of the shock tangential to the shock front (solid line) and $v_{sh,n}$ normal to the shock front (dotted line) in the Sun's frame in the $\alpha = 0°$ direction as functions of time after the launch of the CME. The tangential shock speed initially decreases from $v_{sh,t} \approx 600$ km s^{-1}, to 520 km s^{-1}, then stays constant from $t = 22$ to 36 min. After that time, $v_{sh,t}$ increases steeply to about 840 km s^{-1} at about $t = 43$ min. This acceleration is then followed by a significant drop of $v_{sh,t}$ to about 640 km s^{-1}, after which the shock slowly accelerates again. This nonuniform acceleration history of the shock reflects the nonuniform history of the expanding CME, as shown by the time-varying speed v_{CME} of the CME centroid, which is subject to varying magnetic buoyancy forces as it travels upward in the solar corona [see *Schmidt and Gopalswamy*, 2008]. The increases and decreases of $v_{sh,t}$ follow approximately the time-lagged increases and decreases of the CMEs radial core speed v_x, which is the upper dashed line in Figure 5. Note that the time-lagged increases in $v_{sh,t}$ can be larger than the increases of v_x, when the local plasma parameters at the location of the shock allow it. On the other hand, $v_{sh,n}$ is much smaller than $v_{sh,t}$, starting near 240 km s^{-1} and then decreasing quite uniformly to a value of about 210 km s^{-1} at the end of the temporal evolution. This behavior is consistent with CME expansion driving the shock slowly in the normal direction, with an expansion rate that decreases over time due to adiabatic cooling of the core plasma during this expansion. The CME driving the shock can be detected with a nonzero lateral expansion speed of the CME v_z, which is the lower dashed line in Figure 5. The dominance of $v_{sh,t}$ over $v_{sh,n}$ reveals that the CME driving the shock is primarily a ballistic object in the solar corona. This means that the shock moves relatively slowly in the normal direction on the flanks.

[21] After we have determined the velocity of each location of the shock, we can apply the Rankine-Hugoniot conditions in the rest frame of the shock in order to determine the magnetic field, electron temperature, and cross shock potential jumps $\Delta\mathbf{B}$, ΔT_e, and $\Delta\Phi'$ throughout the shock at each of these locations, using the Alfvénic and sonic Mach numbers found in the shock region. These quantities are required as input parameters for the radio emission calculation developed in sections 2, 3, and 4 of paper 1.

5. Radio Emission Mapping

[22] With known magnetic field, electron temperature, and cross shock potential jumps throughout the shock in the rest frame of the shock, and known magnetic field and velocity field orientations with respect to the shock normal in the rest frame of the shock, reflection efficiencies and reflected velocity distributions can be calculated for kappa velocity distributions of the background electrons, as detailed in section 2 of paper 1. For these reflected electron beam velocity distributions, the so-called plateaued electron distributions resulting from growth of Langmuir waves can be calculated analytically. The properties of the plateaued electron beams are then used to compute the energy transfer into the beam-excited Langmuir waves and the theoretical radiation emissivities induced by the resulting Langmuir turbulence, as summarized in section 4 of paper 1. Readers are referred to paper 1 for detailed formulae.

[23] Figure 6 shows the total electron velocity distribution (solid) predicted on the northern fringe of the shock in the $\alpha = 0°$ direction 20 min after the launch of the CME. The

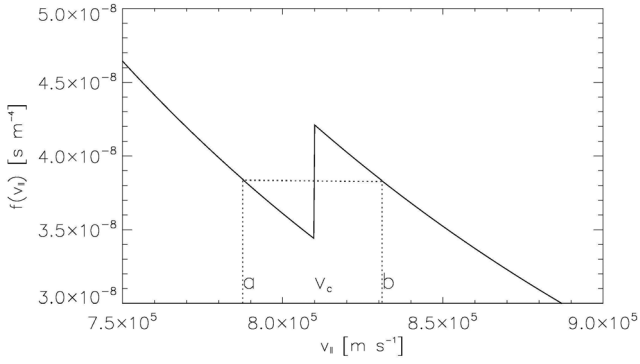

Figure 6. Predicted total electron velocity distribution (solid line) on the northern flank of the shock at $\alpha = 0°$, just upstream of the shock and 20 min after the launch of the CME. The dotted horizontal line is the beam distribution after plateauing, with parameters $a = 788$ km s^{-1}, $v_c = 810$ km s^{-1}, and $b = 831$ km s^{-1}.

dotted curve is the predicted rectangular distribution of the relaxed beam after quasi-linear relaxation (or plateauing) has taken place. The plateau has edge parameters a = 788 km s^{-1} and b = 831 km s^{-1}. The height of the plateau is $\approx 3.85 \times 10^{-8}$ s m^{-1}. The cutoff speed $v_c = v_d \tan \theta_{bn}$ = 810 km s^{-1} in this case, where v_d is the $\mathbf{E} \times \mathbf{B}$ drift speed of the electrons upstream of the shock, and θ_{bn} is the angle between the magnetic field and the shock normal at the location of the shock, respectively. Cutoff speeds exceeding about two times the thermal electron speed v_e lead to effective Langmuir wave excitation [e.g., *Knock et al.*, 2001]. In this example $v_e \approx 400$ km s^{-1}.

[24] From the position of a given point on the flank shock front, the excited electron beam is followed along a trajectory whose local velocity vector is determined by the value of the nearly constant beam speed v_b in the direction of the local magnetic field **B**, which varies along the path, plus the local $\mathbf{E} \times \mathbf{B}$ drift velocity of the electrons $\mathbf{v}_d = -[\mathbf{u} \times \mathbf{B}] \times \mathbf{B}/B^2$, which also varies along the path. Here $\mathbf{u} = \mathbf{v}_{sw} - \mathbf{v}_{sh}$ is the plasma velocity upstream of the shock in the rest frame of the shock, and $\mathbf{v}_{sw}$ and $\mathbf{v}_{sh}$ are the solar wind velocity and the shock velocity in the rest frame of the Sun, respectively (also compare with section 3 of paper 1). The necessary parameters for these velocities are calculated for each point of the trajectory, with $v_b = \frac{1}{2}(a + b) \approx 809$ km s^{-1} in the example given in Figure 6. Hence, the trajectory of the electron beam and so the source location of its radiation are determined self-consistently. After the computation of the full velocity field for the trajectories of the electron beams in the upstream region of the shock and in the rest frame of the shock, this velocity field is then Galileo transformed to the rest frame of the Sun, where the beam trajectories are computed in order to map the radiation source in the rest frame of the Sun.

6. Radio Emission Results

[25] Our simulation results are displayed in Figures 7–11. Figure 7 shows examples of the volume emissivities (power per unit volume) $j_F(\omega_p)$ and $j_H(2\omega_p)$ of fundamental and harmonic radiation, respectively, at specific times on the flanks of the shock. Figures 8 and 9 are blown-up images of $j_H(2\omega_p)$ in the Northern and Southern Hemispheres at an early time. Figure 10 shows the distribution of T_e (**r**) near the CME and shock, very useful for interpreting the variations of $j_H(2\omega_p)$ and $j_F(\omega_p)$ with position.

[26] Figure 11 shows the contributions to the total flux density coming from the flank shocks in the Northern (Figures 11a and 11b) and Southern Hemispheres (Figures 11c and 11d) for harmonic (Figures 11a and 11c) and fundamental emission (Figures 11b and 11d). Figure 12 shows the integrated flux density of the shock-excited radiation from near the nose of the shock, as already discussed in paper 1, and with the bands labeled N-A and N-B identifying harmonic and fundamental emissions, respectively. Finally, Figure 13 displays the total flux density for the whole shock, including contributions from the flank and nose regions. Bands N-A, N-B, A,B, and C,D identify fundamental and harmonic radiation from the nose and flank regions with the same labeling as in Figures 11 and 12.

[27] Figure 7a shows the color-coded volume emissivity $j_H(2\omega_p)$ for harmonic radio emission predicted upstream of the CME-driven flank shock in the x-z plane, 20 min after the launch of the CME. The maximum volume emissivities are near 10^{-17} W m^{-3} sr^{-1}, leading to maximum predicted total flux densities for fundamental and harmonic plasma emission in the range 10^{-20}–10^{-18} W m^{-2} Hz^{-1} at Earth's orbit, depending on the relevant source volume and distance. This is consistent with observations like those of *Bale et al.* [1999], who measured flux densities $F_F \sim 10^{-18}$ W m^{-2} Hz^{-1} and $F_H \sim 10^{-20}$ W m^{-2} Hz^{-1} for fundamental and harmonic radiation, respectively, in the frequency range $f \sim 10^5$–10^6 Hz, and other simulations like *Knock and Cairns* [2005] and *Cairns and Knock* [2006].

[28] The core of the CME is marked with the red circle centered on the x axis in Figure 7. The red and the blue polygonal lines show the spatial positions of the CME-driven shock, obtained by applying the shock capturing procedure described in section 2 above for different α. The blue line corresponds to the max positions defined in Figure 3, and the red line corresponds to the kink positions. These are polygonal lines rather than smooth lines since we determine the max and kink position in the density profiles for various α and then connect neighboring points with straight lines. The shock ramp lies between the blue and red lines.

[29] We see that for $0° \geq \alpha \geq -55°$ and $180° \geq \alpha \geq 235°$ the blue and red lines are roughly arcs of an ellipse, though distorted by ripples and wiggles. These ripples and wiggles have larger amplitudes for $\alpha \approx -55°$ and $\alpha \approx 235°$. The average spatial scale of such ripples is about 0.2 $R_\odot$, and their average lifetime (or temporal scale) about 10 min. One obvious mechanism that can start the development of these ripples and wiggles in the shock front is the interaction between intrinsic solar wind turbulence and the shock. A second is the development of turbulence in a broad layer around the body of the CME: as the CME moves into the solar wind, the CME-driven shock evolves, and information propagates from the CME to the shock and vice versa through a layer that moves slower than a fast-mode wave. This turbulence increases in magnitude to the rear of the object. The turbulence level is also larger in the Northern Hemisphere where reconnection of magnetic field lines

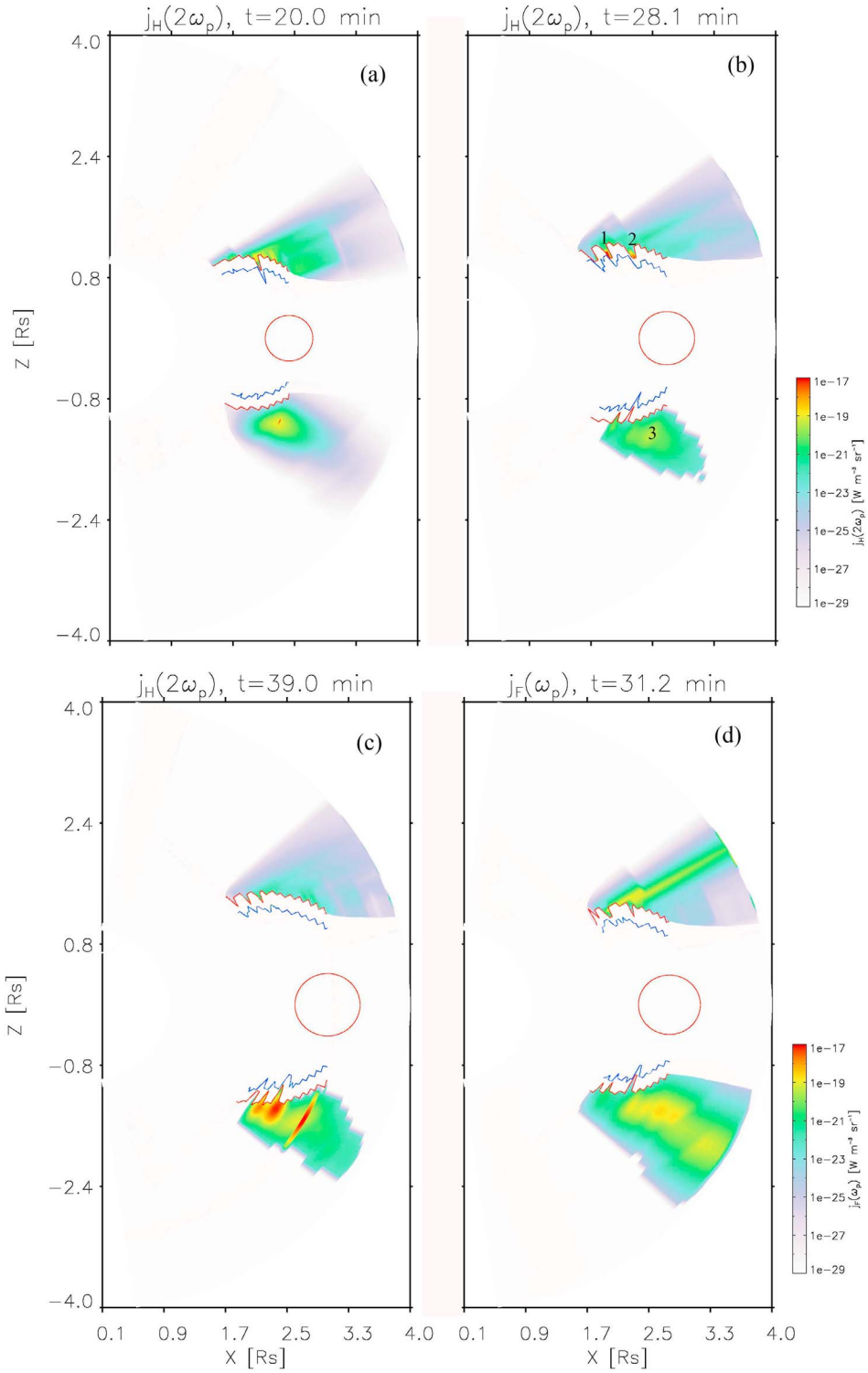

Figure 7. Plots showing (a) $j_H(2\omega_p)$ at t = 20.0 min, (b) $j_H(2\omega_p)$ at t = 28.1 min, (c) $j_H(2\omega_p)$ at t = 39.0 min, and (d) $j_F(\omega_p)$ at t = 31.2 min. The region between the blue and red curves is the ramp region of the shock. The brightest emission regions in Figure 7b are marked by numbers 1–3.

occurs, as indicated by a clear reconnection x point of magnetic field lines in that area in Figure 1a (see *Schmidt and Cargill* [2003] for a detailed discussion). The ripples are not stationary. Instead, they move slowly to more rearward positions with increasing time, thereby evolving their depth and spatial dimensions as seen in Figure 7. Additional possible mechanisms that can enable the development and movement of ripples are the occurrence of an instability at locations on the shock front like the Rayleigh-Taylor or the Kelvin-Helmholtz instability. All of these effects would allow

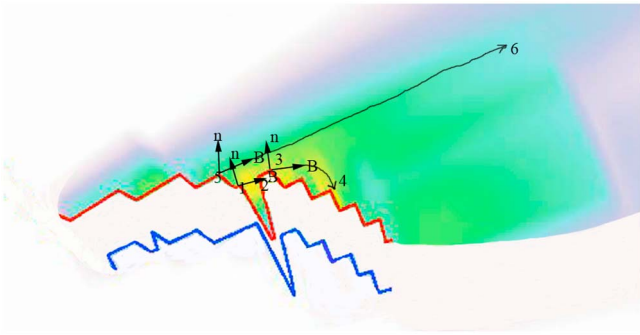

Figure 8. Expanded version of Figure 7a for the Northern Hemisphere, with the same color bar.

the ripples to evolve over time and spread toward the rear of the CME-shock system if the ripple propagation speed is small compared with the CME speed and the fast mode or other MHD phase speeds.

[30] Regarding the electron $\mathbf{E} \times \mathbf{B}$ drift speed we can conclude the following: From Figure 5 we can see that the shock velocity $\mathbf{v}_{sh}$, although mainly tangentially directed to the shock front, still has a component $v_{sh,n}$ normal to the shock front, which is directed almost perpendicular to the radial direction. Since the solar wind velocity $\mathbf{v}_{sw}$ is mainly radially directed, $\mathbf{v}_{sw} - \mathbf{v}_{sh}$ has a component $\approx -\mathbf{v}_{\mathbf{sh,n}}$ directed toward the shock front. With an almost radially directed magnetic field in the upstream region of the shock, the electron drift speed, which is the plasma velocity perpendicular to the local magnetic field in the rest frame of the shock, $\mathbf{v}_d = -[(\mathbf{v}_{sw} - \mathbf{v}_{sh}) \times \mathbf{B}] \times \mathbf{B}/B^2 \approx - v_{sh,n}\mathbf{n}$, where $\mathbf{n}$ is the shock normal. Thus, we have an $\mathbf{E} \times \mathbf{B}$ electron drift that has a component toward the shock, which is a result independent of the magnetic field magnitude. Different magnitudes of v_d can make beams of a specific v_b more closely follow the $\mathbf{B}$ lines when v_d/v_b is smaller.

[31] The calculation of the electron beams that excite the radio emission starts at locations along the red demarcation line (Figure 7). The ripples and wiggles of the shock front can have a significant effect on the intensity of the radiation.

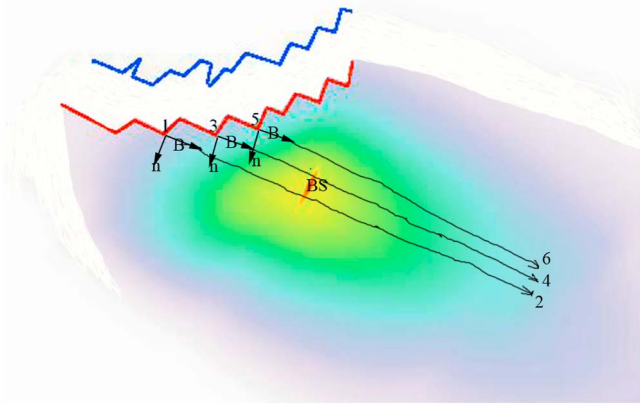

Figure 9. Expanded version of Figure 7a for the Southern Hemisphere, with the same color bar.

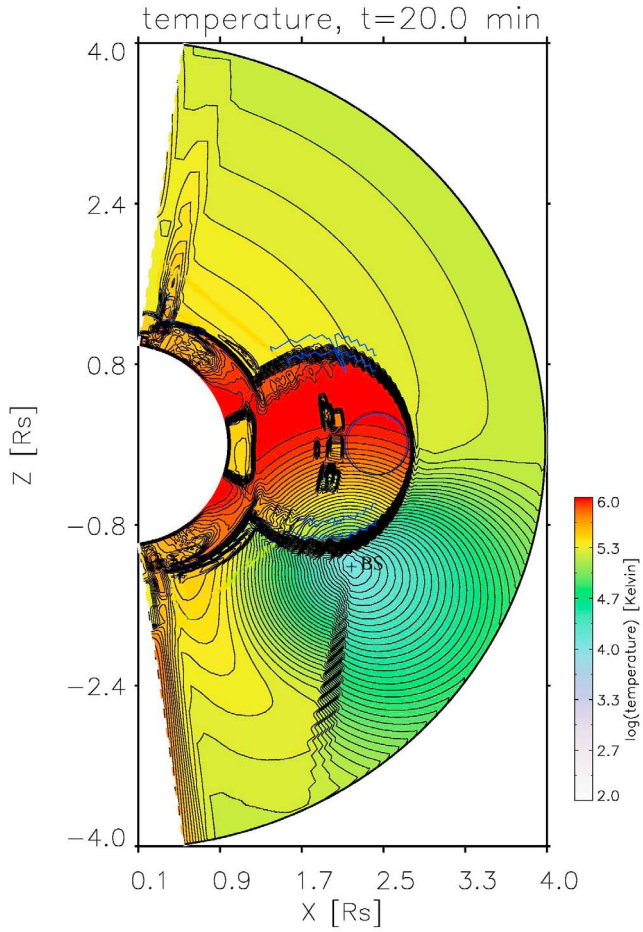

Figure 10. Temperature distribution in and around the CME-driven shock at $t = 20$ min, color coded and with black contour lines. Blue lines show the boundaries of the upstream/downstream regions, corresponding to the kinks and max positions in Figures 3 and 4; the inner and outer blue lines are obscured by the block contour lines in the northern and southern flanks, respectively. BS identifies the bright spot in $j_H(2\omega_p)$ in Figures 7a, 7b, and 9.

Along a border of such a ripple, the shock normal $\mathbf{n}_{sh}$ turns its direction relative to the local magnetic field $\mathbf{B}$, as the shock front turns direction for different α. At specific positions, the shock normal becomes almost perpendicular to the magnetic field. These are the positions where the excitation of the fastest electron beams occur, since the cutoff speed increases as θ_{bn} tends to 90°. Strong and fast electron beams, then, can excite strong radio emission in a local area originating from where $|\theta_{bn} - 90°| \leq 10°$ [*Knock et al.*, 2001, 2003b], which can be denoted as a bright spot along the border of the shock wave.

[32] Given the fact that the $\mathbf{E} \times \mathbf{B}$ drift velocity of the electrons is always directed toward the shock front according to our previous discussion, this drift keeps the electron beams between the shock front and the magnetic field lines tangent to the shock.

[33] A prominent feature in Figures 7a and 8, which is a blown-up figure of the northern part of Figure 7a, is the following: Near the point 1 in Figure 8, which has $\alpha \approx -15°$,

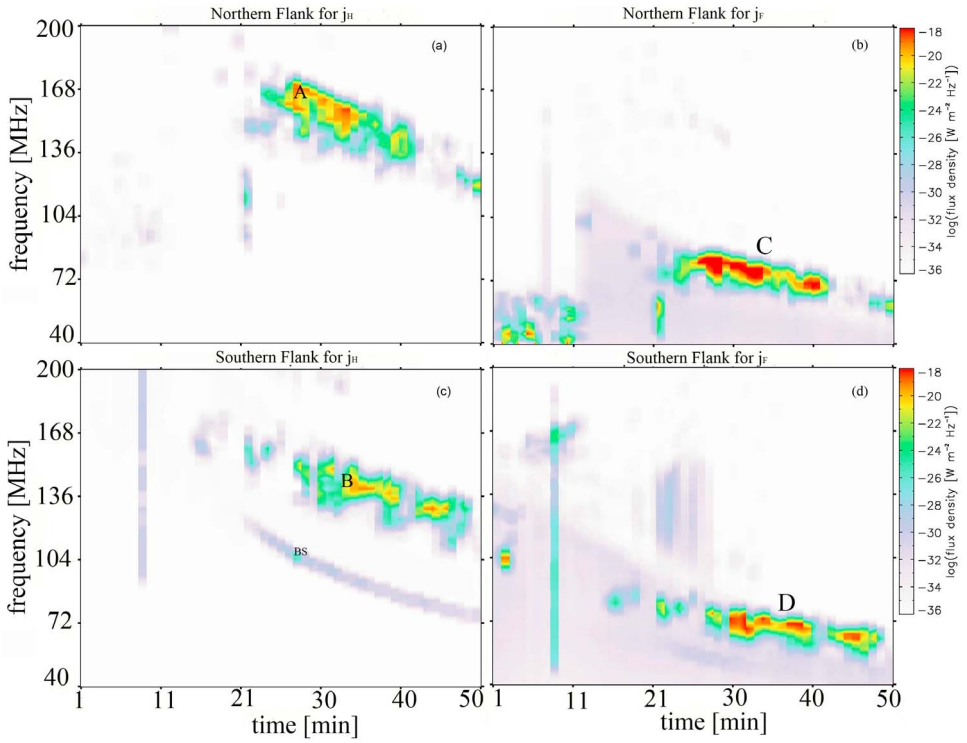

Figure 11. Dynamic spectra of the emission as functions of shock location and emission mode: northern flank for (a) harmonic and (b) fundamental emissions; southern flank for (c) harmonic and (d) fundamental emissions.

we have a pronounced trough or ripple in the shock front. At the outer western edge of the trough along the red polygon line, position 1, the magnetic field **B** is almost perpendicular to the shock normal **n**. The result is fast electron beams from that part of the shock front, which leads to maximum volume emissivities around 10^{-21} W m^{-3} sr^{-1}. The line connecting point 1 with point 2 in Figure 8 is a calculated electron beam path emerging from point 1 on the

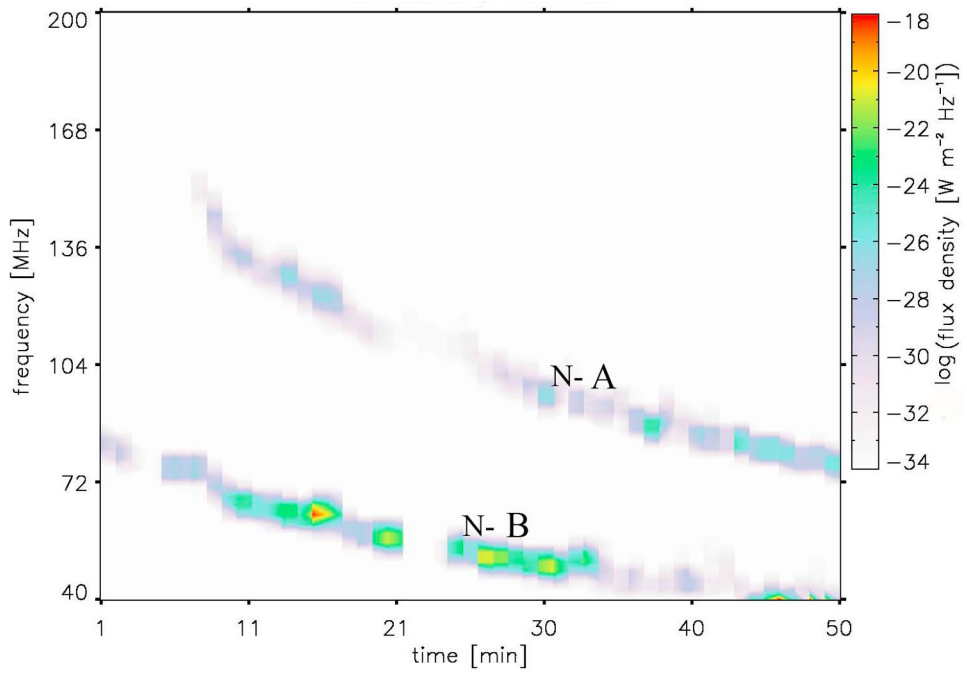

Figure 12. Dynamic spectrum of the flux density from upstream of the nose region of the shock, with $\alpha \in (30°, 150°)$.

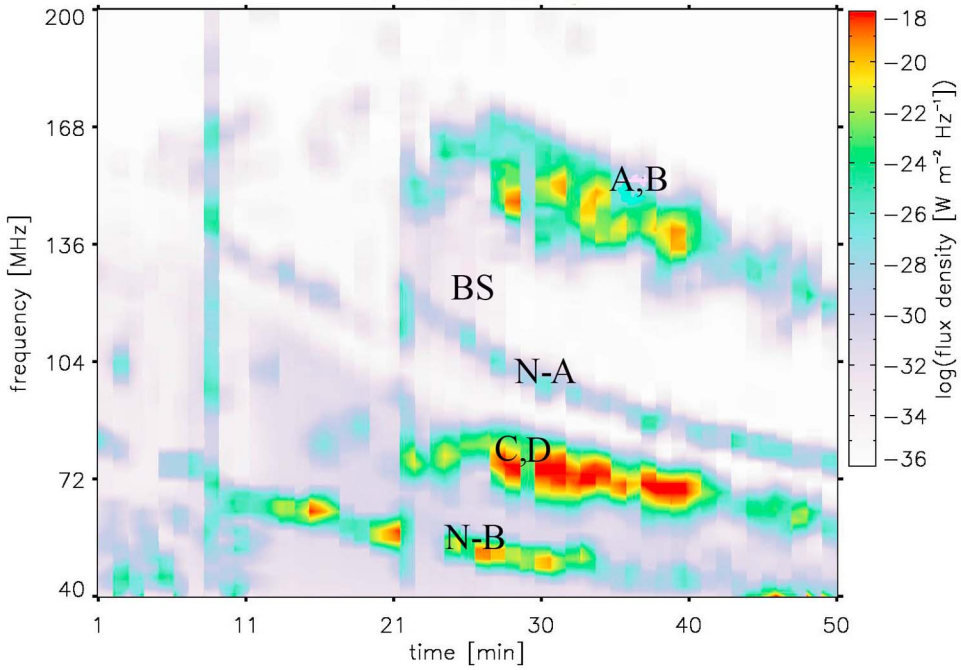

Figure 13. Total flux density. Labels N-A and N-B identify harmonic and fundamental radiation from the nose region, respectively. Labels A,B and C,D identify harmonic radiation and fundamental radiation, respectively, summed over the northern and southern flanks. Label BS denotes band BS in Figure 11c.

shock front. This electron beam path turns southward away from the magnetic field direction, eventually coming close to the ramp region of the shock between the red and blue polygon lines. This behavior is a consequence of the strong southward directed electron drift velocity and a small ratio v_b/v_d. We find radio emission excitation in the area surrounding the beam. Further reflection and transmission of this electron beam by the shock ramp near point 2 is not considered here.

[34] We find a quite similar situation at the western edge of the neighboring trough of the adjacent ripple in the eastern direction, labeled with point 3 in Figure 8. Again, **B** denotes the local magnetic field direction, and **n** the local shock normal at point 3. We see that **B** and **n** have an angle θ_{bn} which is not far from 90°, thus providing conditions for a reasonable electron acceleration and creating a bright spot in the radiation field to the right of position 3. Here, bright spot means "bright radio emission," which is either due to a fast beam (with the condition v_b/v_e or v_b/v_d is large) or due to a strong beam (with the condition n_b/n_0 is large). The line connecting point 3 with point 4 is the calculated electron beam path that starts from point 3. Again, this path is directed southward to the magnetic field direction due to the large southward electron drift, finally leading close to the ramp region of the shock. This shows that the ratio v_b/v_d is not too large for this particular beam. However, we find a larger ratio n_b/n_0 for this particular beam compared with beams originating from nearby shock front elements without ripples.

[35] We find a different situation for the electron beam launched from position 5 in Figure 8. Here, the angle θ_{bn} between **B** and **n** is less than 90°, yet still large enough (≥85°) to provide for reasonable electron acceleration. Quite obviously, v_d is not so strong here. In consequence, the excited electron beam, moving along the calculated path connecting point 5 with point 6 in Figure 8, follows the radial external magnetic field lines quite closely, which is an indication for a large ratio v_b/v_d. This and similar almost radially propagating beams are responsible for the extended radiation field, which stretches in front of the shock along **B** in Figure 8. Such electron beams could also be related to type II herringbones and/or SA type III bursts [e.g., *Holman and Pesses*, 1983; *Mann and Klassen*, 2005; *Dulk et al.*, 2000].

[36] In Figure 9, which is a blown-up figure of Figure 7a in the Southern Hemisphere, we display j_H $(2\omega_p)$ at the southern fringe of the CME-driven flank shock 20 min after the launch of the CME. Here, the shock segments at the onset of the upstream region (red line) and at the edges of the shock ripples stretching to the west of each point 1, 3, and 5, have a shock normal **n** that is almost perpendicular to the local magnetic field **B** intersecting the shock. Hence, fast electron beams are launched from segments 1, 3, and 5 in the **B** direction. There is only a relatively small electron drift velocity directed toward the shock. Thus we see little deflection of the electron beams from the almost radial magnetic field direction. This is evident for the simulated electron beam paths connecting points 1, 3, and 5 with points 2, 4, and 6 in Figure 9.

[37] In Figure 7c and Figure 9 bright emission regions abruptly develop far from the shock, despite the general theoretical expectation that the relative beam density and so the levels of Langmuir waves and radio emission will decrease with increasing distance from the shock [e.g., *Knock*

et al., 2001, 2003b; *Cairns*, 2011]. As shown next, these enhancements develop due to changes in the plasma environment experienced by the electron beams (specifically, localized decreases in T_e) which increase the ratio v_b/v_e and the volume emissivities of f_p and 2 f_p radiation.

[38] In Figure 10 we display the color-coded temperature distribution in the simulation box 20 min after the launch of this particular simulated CME. The position of the core of the CME is marked with a blue circle. The lines that mark the boundaries of the upstream/downstream regions of the CME-driven flank shocks in the Northern and Southern Hemisphere, which are defined as the kink/max positions of the density profile in our simulation box, are plotted with blue curves. A roughly ellipsoidal area which includes the core of the CME, and whose northern (southern) edge approximately coincides with the demarcation line for the downstream (upstream) region of the flank shock in the Northern (Southern) Hemisphere, respectively, has a temperature of predominantly 10^6 K. However, the southern part of this ellipsoidal area is cooler than the northern part, with a temperature $\approx 10^5$ K. Thus, this northern ellipsoidal high-temperature area is in fact limited within the ramp region of the CME-driven shock. (It is not a contradiction that the region with a large temperature gradient, which is the area with very concentrated black contour lines, extends to about the middle of the ramp region in the Northern Hemisphere but lies outside the shock in the Southern Hemisphere, because these contour lines correspond to much lower temperatures in the Southern Hemisphere.)

[39] Obviously, the ellipsoidal area constitutes an expanding bubble of hot plasma released in the solar eruption which becomes the CME, and upstream of which the CME-driven shock develops. During its temporal evolution, the northern and southern parts of this expanding plasma bubble are heated differently. In the northern part, where the magnetic field lines of the CME and the coronal plasma are antiparallel, reconnection leads to a dissipation of magnetic energy and thus to a heating of the plasma. This heating is lacking in the Southern Hemisphere, where the magnetic field lines of the CME and coronal plasma are parallel and so do not reconnect. Hence, we obtain a negative temperature gradient when we look from the north to the south in our simulation box. The general decrease of the temperature in the radial direction outside the plasma bubble is due to the adiabatic cooling in a spherically expanding solar wind plasma. In the Southern Hemisphere, the lack of a heating due to reconnection leads to a coolish area adjacent to the CME eruption, where the minimum temperature at the point labeled with BS in Figure 10 is about 10^4 K in our particular simulation. While this is much lower than believed normal in the corona, as discussed in section 7, note that HELIOS has measured electron temperatures as low as 10^4 K at heliocentric distances between 0.3 and 1 AU (see, e.g., *Pilipp et al.* [1987, Figure 2] for an explicit example of HELIOS electron temperature measurements around 0.9 AU), which is $\approx$1/20 of the electron temperature at 0.3 AU where the average $\langle T \rangle$ is between $\approx 2 \times 10^5$ K and $\approx 4 \times 10^5$ K. The point BS stands for bright spot and is coincidental with the point BS is Figure 9, where we find the maximum emissivity in the radiation field south of the CME-driven flank shock. The occurrence of such a spot suggests that more favorable plasma conditions for excitation of radio emission exist some distance away from the shock front in the Southern Hemisphere. A decrease in T_e causes a decrease in v_e, where $v_b \approx v_c \geq 2v_e$ is the criterion for effective excitation of Langmuir waves. Thus a smaller v_e with essentially the same cutoff speed v_c is expected to lead to a beam with larger v_b/v_e and so higher levels of Langmuir waves. This amplifying effect is counteracted by the increased distance from the shock, since the available free energy for Langmuir growth decreases inversely with distance from the shock [*Knock et al.*, 2001; *Schmidt and Cairns*, 2012]. The conversion efficiencies for fundamental and harmonic radiation via the foregoing nonlinear Langmuir processes and therefore the plasma emissivities roughly depend on $T_e^{3/2}$ [*Knock et al.*, 2001, 2003a]. Thus, the temperature dependency of $j_F(\omega_p)$ and j_H $(2\omega_p)$ is not very strong. The combined result is a bright spot in front of the shock front, which is denoted with BS in Figure 9 and corresponds to the minimum in T_e, maximal growth of Langmuir waves, and to a local maximum $j_H(2\omega_p) \approx 10^{-17}$ W m^{-3} sr^{-1}. Without such additional structure in T_e (**r**) we expect j_F (**r**) and j_H (**r**) $\rightarrow$ 0 with increasing distance from the connection point on the shock, as seen in Figures 7–10, due to the decrease in available free energy for Langmuir growth not being sufficiently compensated by the decrease in T_e (**r**) at larger distances from the shock.

[40] In Figure 7b we display the radiation field $j_H(2\omega_p)$ 28.1 min after the launch of the CME. The flank shock has further evolved, typically becoming stronger. There are much deeper ripples in the flank shock front, with the deepest ripples closer to the rear of the flank shock. Generally, the growth in the strength of the shock leads to more intense radio emission, as found elsewhere [*Knock et al.*, 2003a, 2003b]. In the Northern Hemisphere, we can see two bright spots, labeled with 1 and 2 in Figure 7b and situated very close to the shock ripples, as we have discussed in connection with Figure 8. These bright spots emit quite intensely, with $j_H(2\omega_p) \approx 10^{-17}$ W m^{-3} sr^{-1}. Culgoora and Nançay radioheliographic observations [e.g., *Prestage*, 1994; *Maia et al.*, 2000] and interplanetary observations [e.g., *Reiner at al.*, 1998; *Hoang et al.*, 2007] have indeed shown that type II bursts are excited in localized sources, frequently near the flanks of erupting structures.

[41] The integrated radio signal coming from these bright spots can be found in area A of Figure 11a, which shows the total flux density of harmonic radiation coming from the northern flank of the shock. In area A the maximum flux densities are around 10^{-18} W m^{-2} Hz^{-1}, spread over a frequency range of about 15 MHz and with more than one peak in frequency at a given time. This multipeak structure is due to there being more than one bright spot on the northern fringe of the shock wave at this time. Each bright spot corresponds to the electron paths from a specific ripple on the shock front with slightly different plasma densities, thus emitting at slightly different values of f_p and $2f_p$. The burstiness of these bright spots is due to (1) the varying locations of the temporally developing shock ripples and electron paths, and (2) varying intensities of the bright spots due to temporal changes in the directions of the shock normals with respect to the local magnetic field direction for the ripples, which modulate the effectiveness of these regions on the shock front in accelerating electrons. Thus, the multipeak structure of the dynamic spectrum identified in area A in

Figure 11a changes with time and frequency. These variations lead to a broadened and bursty emission band rather than a thin line in the dynamic spectrum. The correlation of fine structures in the emission bands with ripples on the shock qualitatively supports the role of ripples identified in the work of *Knock et al.* [2003b], *Knock and Cairns* [2005], *Cairns and Knock* [2006], and *Hillan et al.* [2012a, 2012b].

[42] In the Southern Hemisphere, the bright spot ahead of the shock front, as indicated with 3 in Figure 7b, has weakened by time 25 min. Please note that the majority of region 3 still has $j_H \approx 10^{-20}$ W m^{-3} sr^{-1}, which is much less than the volume emissivity of about 10^{-17} W m^{-3} sr^{-1} near ripples 1 and 2 in the same figure. Therefore, the contributions of the regions BS and 3 in Figures 7a and 7b lead to a weaker signal in the dynamic spectrum of Figure 11c, labeled with BS, than the contributions labeled with A in Figure 11a that are due to ripples 1 and 2 in Figure 7b. This is despite the flux being an integral over the volume emissivity with a distance related falloff. The much larger volume of the region BS and 3 in Figures 7a and 7b is not able to compensate for the much lower volume emissivities.

[43] The majority of the regions BS and 3 in Figures 7a and 7b has a smaller plasma density than near the shock front, due to the spherical expansion of the solar wind. Hence, band BS in Figure 11c is at lower frequencies than the much broader and burstier bands A and B in Figures 11a and 11c which correspond to ripple activity on the northern and southern shock fronts. The drifts of bands BS, A and B reveal the decrease in the plasma density of the emitting regions as the CME moves out of the solar corona. Hence, such bands can be used to infer plasma density profiles in the solar corona ahead of erupting CMEs. Such bands also contain information on how the dominant emitting regions evolve with time along the macroscopic shock and also well upstream of the shock (see Figures 7–10). Thus, it is not a simple matter to relate the drift of an emission band to a single shock or CME velocity and a single radial density model [see also *Knock and Cairns*, 2005; *Cairns*, 2011].

[44] In Figure 7c, which shows the radiation field for $j_H(2\omega_p)$ 39.0 min after the CME launch, the ripples in the CME-driven shock front that have the largest depths have moved further toward the rear of the CME. Since such a movement has the tendency to turn the direction of ripple shock normals away from a direction perpendicular to the local magnetic field, the general effect is a slow weakening of the radiation field. We can detect this effect in the bands A and B in Figures 11a and 11c, which decrease in intensity until about 40 min. In addition, the features 3 and BS in Figures 7a, 7b, and 9, respectively, have evolved to a narrow partial arc of a circle in Figure 7c.

[45] Finally, Figure 7d shows the volume emissivity of fundamental radiation, $j_F(\omega_p)$, 31.2 min after the launch of the CME. This is close to the onset of significant fundamental radio emission from the southern flank as can be seen in the dynamic spectra for fundamental emission in Figures 11b and 11d. The features of fundamental emission, with time-dependent shock ripple modulations and more extended regions of slowly varying emissions (as in Figure 7d), are very similar to the features for harmonic emission in Figures 7a–7c. Again, the result are two overlapping bursty multipeaked broad bands in the dynamic spectrum in Figures 11b and 11d, belonging to northern and southern flank radiation, plus a weak band corresponding to the region BS. Note that the vertical lines and other islands of small emission in the Figures 11a–11d are weak radio noise that is generated at density fluctuations that are misidentified as weak shocks.

7. Discussion

[46] Throughout our simulation we find that the ramp of the CME-driven flank shocks, between the red and blue lines in Figures 7–9, which denote the boundaries between the upstream and downstream regions, respectively, spread out over three or more cells in our simulation box. This is a macroscopic ramp width, whereas in reality the ramp width should be microscopic in size, on the order of about one ion gyroradius. So in the limit of an ideally steepened shock front, the red and blue demarcation lines should almost coincide. This is why we do not calculate radio emission coming from the ramp region of the shock. Similarly, we do not calculate emission from downstream of the shock ramp [*Cairns*, 2011]. Hence, we have calculated the simulated radiation field starting outside the red demarcation line for the upstream region. It should be mentioned, however, that it is possible that electrons which are reflected from a rippled shock can move along the field lines to another region of the shock and enter into the downstream region. Since such reflected and accelerated electrons have smaller pitch angles than when they were incident on the first region of the shock, it is possible that many would not be reflected at the second region, thereby perhaps leading to an electron beam and so emission in the downstream region, too. This might be one way to obtain emission from upstream and downstream of the shock, as in a frequent interpretation of band splitting [*Smerd et al.*, 1974; *Vršnak et al.*, 2001; *Magdalenić et al.*, 2002]. This specific mechanism for downstream emission identified here relies on having a rippled shock and sufficiently curved magnetic field lines so that many magnetic field lines intersect the shock front more than once. This idea needs to be quantified.

[47] The bright spots identified to the right of points 1 and 3 in Figure 8 lead to flux densities on the order of 10^{-18} W m^{-2} Hz^{-1} in Figure 11a for our particular simulation. The rest of the source region in Figure 8, with volume emissivities around 10^{-21} W m^{-3} sr^{-1}, leads to flux densities on the order of 10^{-21} W m^{-2} Hz^{-1} in Figure 11a for our particular simulation. The significant increase in the flux density that ripples provide here with respect to the flux densities for an unrippled shock front, shows that naturally developing ripples on the shock are often very important in producing type II emission. These naturally developing ripples provide a natural link between the ripple theory of *Knock et al.* [2003b], *Knock and Cairns* [2005], *Cairns and Knock* [2006], and *Hillan et al.* [2012a, 2012b], and our bolt-on model.

[48] In Figure 12 we display the flux density upstream of the nose region of the shock, as already discussed in *Schmidt and Cairns* [2012]. The label N-A denotes the harmonic emission band in this figure, and label N-B the fundamental emission band. Both bands are hyperbolic curves due to a $1/r$ dependency of the plasma frequency with the radial

heliocentric distance r at the location of the nose shock front, which is a consequence of the r^{-2} decrease of the plasma density with r in a spherically expanding solar wind. At about 21 min after the launch of the CME we see a temporal fading of the emission lines, which is caused by a temporal decrease of the magnetic buoyancy forces on the core of the CME that allows the CME to decelerate. In consequence, the CME-driven front shock weakens. The weaker shock is less effective in accelerating electrons and thus leads to weaker reflected electron beams and so lower levels of Langmuir waves. When the magnetic buoyancy forces on the CME become larger again, the CME-driven front shock steepens again, and the type II emission lines strengthen again. Maximum flux densities are in the order of 10^{-22} W m^{-2} Hz^{-1} for the harmonic emission band N-A, and 10^{-20} W m^{-2} Hz^{-1} for the fundamental emission band N-B.

[49] We can also find the bands N-A and N-B of Figure 12 in Figure 13, which displays the total flux density from the macroscopic shock for fundamental and harmonic emission. The multiple band (or "multiple lane") spectrum results from radio emission excited from different shock regions in both the fundamental and harmonic modes. In Figure 13, band A, B is the contribution of the northern and southern flank shock to the harmonic emission. We find flux densities of up to 10^{-18} W m^{-2} Hz^{-1} in band A,B, which is much larger than the harmonic nose flux density of emission line N-A. The band BS in Figure 11c, which was interpreted earlier in terms of enhanced emission in front of the southern flank shock due to a preexisting local depletion of the temperature in Figure 9, partly overlaps with emission line N-A in Figure 13. This BS band fills the gap in the emission band N-A after 21 min, yet with a shift to higher frequencies at the later end of the gap.

[50] The band C,D in Figure 13 is the superposition of bands C and D displayed in Figures 11b and 11d for northern and southern fundamental flank emission. The flux density in band C,D is often about 10^{-18} W m^{-2} Hz^{-1}, again exceeding the fundamental nose flux density of emission band N-B most of the time.

[51] We would expect a measured spectrum to often look like the simulated spectrum of Figure 13 and so be composed of multiple bands, and so reminiscent of the multiple lane type II bursts sometimes observed [*Nelson and Melrose*, 1985; *Cairns*, 2011]. Our discussion above shows how this complicated total dynamic spectrum can be decomposed into emission from different spatial regions and the different emission mechanisms of fundamental and harmonic radiation.

[52] The discussion above also shows that there can be very significant and sometimes dominant emission from the flanks of the macroscopic shock, despite the shock moving primarily ballistically. Previously, *Stewart and Magun* [1980] and *Holman and Pesses* [1983] have postulated, and *Knock and Cairns* [2005] have found in simulations, that flank regions of shocks rather than the nose of the shocks can produce most or all of an observed type II burst.

[53] Our simulation and that of *Knock and Cairns* [2005] show that it is difficult to obtain the actual radial speed of a propagating CME and shock wave from the observed drifting bands of type II emission. Instead, when the radiation predominantly comes from flank regions of the shock the drifting emission frequency does not correspond to the radial speed of the shock nose but instead to a combination of a speed of the active source region across the shock surface and to the shock's overall radial speed. This difference must be taken into account in order to derive correct CME speeds from the drift rate of type II bands, a question crucial for space weather applications. Model calculations like ours, and fits to observed events [*Hillan et al.*, 2012a, 2012b], can be used to solve this difficult task and in principle derive precise CME speeds from type II burst observations.

[54] Another possible application of our simulations exploits the idea that the timescale for the appearance and evolution of ripples corresponds to the timescale of the burstiness of the dynamic spectrum. Thus, one can probe ripples via timescale analyses of the resulting dynamic spectrum.

[55] The CME and associated radio calculations reported here are only initial work, and are not intended to model particular events or be fully realistic. In particular, plasma temperatures as low as 10^4 K within 4 $R_\odot$ are unrealistic for the corona and inner solar wind. Instead, we would expect the shock to propagate into a heated coronal and solar wind plasma that has temperatures of order 10^6 K. Higher solar wind temperatures would require higher cutoff speeds at the shock front to produce significant radiation. Future simulations will address more realistic coronal and interplanetary conditions. Other options are to design the CME to be more ballistic with a more elongated ellipsoidal body of the CME in the radial direction rather than a nearly circular body, or to introduce coronal magnetic field loops or other magnetic structures whose fields are more perpendicular to the radial direction [e.g., *Knock and Cairns*, 2005]. These would make the shock front near the nose more quasi-perpendicular and thus increase the cutoff speed and radio emission. We can also extend our work into three dimensions by considering more than five cells in the azimuthal ϕ direction and introducing a variation of the fields in the ϕ direction. This would result in a propagating shock that also develops ripples in the ϕ direction, leading to further fine structure in the excited dynamic spectra. Future work will be along these lines.

8. Conclusions

[56] We have applied our new entirely analytic bolt-on model for the electron beams, Langmuir waves, and the radio emission upstream of a shock to an MHD simulation of a CME-driven shock. Our particular focus is on the radio emission excited on the northern and southern flanks of the shock. For that purpose we developed a routine to determine the 3D location of the shock, thereby bounding the upstream and downstream regions of the shock using kinks and relative maxima in the density profile along multiple rays traversing the shock.

[57] Ripples develop due to preexisting and developing turbulence at the location of the shock, and due to plasma instabilities, variations of the Alfvén speed along the shock front, or other shock related physics. Within these ripples there are regions where the shock becomes closely perpendicular. These shock elements are oftentimes the origins of electron beams that propagate with large speed or are quite strong, and are favored to excite radio emission with larger intensity. These locations with greater radio emission can be seen as bright spots in the source images and as intensity enhancements in the dynamic spectrum. The ripples do not stay at the same position on the shock front during the

temporal evolution, instead moving toward the rear of the shock with increasing time. This movement of the bright spots into regions with different density leads to variations of the emission frequency that lead to a multipeaked bursty drifting bands (or lanes) in the dynamic spectrum. In the case that reflected electron beams meet with more favorable plasma conditions for radio excitation farther away from the shock front, e.g., due to a decreasing electron temperature, they can produce observable radiation farther from the shock and so larger bandwidth and more intense drifting bands in the multicomponent dynamic spectrum.

[58] In our simulation, the movement of the bright spots in the source radiation fields, linked with ripples in the shock front, toward the rear of the flank shock and along the northern and southern flanks of the shock has as a consequence that the region of the shock with bright spots slowly becomes less perpendicular due to a slow rotation of the shock normal along the shock front relative to the almost constant magnetic field direction in the flank shock region. This leads to a slow fading out of those bands in the multiple-band dynamic spectrum connected with the bright spot radiation sources. This natural development of ripples on the shock provides a natural link between the ripple theory of *Knock et al.* [2003b], *Knock and Cairns* [2005], *Cairns and Knock* [2006], and *Hillan et al.* [2012a, 2012b] and the bolt-on theory presented here. Thus, ripples are often very important in producing type II emission.

[59] We can use our findings for a more accurate interpretation of observed dynamic spectra for radio type II bursts that have multiple lanes or bands. The slope of the drifting bands connected with bright spots of radio excitation at ripples can be used to derive density profiles of the solar wind at the location of the bright spots, which move along the macroscopic CME-driven shock and may be near the flanks, the nose, or both. The slopes of other bands may correspond to enhancements of the radio flux from regions well upstream of the shock, due to local enhancements in the efficiencies of driving Langmuir waves or radio emissions there, for instance due to variations in T_e like in our simulation. The slopes of the radio bands thus contain information on the 3D density profile, the locations of the radio sources relative to the shock, and the shock's evolving 3D velocity and 3D location [e.g., *Cairns*, 2011].

[60] We find major emission from the flanks for this simulation, consistent with the postulates of *Stewart and Magun* [1980] and *Holman and Pesses* [1983] and with the earlier simulation of *Knock and Cairns* [2005]. Thus, some type II bursts will have their radiation produced primarily on the flanks of the shock, others near the nose, and others both. This complicates the interpretation of observed dynamic spectra considerably.

[61] Future work will be concerned with simulations that have more realistic temperature profiles for the solar corona, more radially stretched magnetic field configurations that enable the CME to erupt more rapidly, solar magnetic fields that have larger components perpendicular to the radial direction, and the full consideration of the evolving radio source in three spatial dimensions.

[62] **Acknowledgments.** Constructive comments from B. Li, V. L. Lobzin, and the referees and support from the Australian Research Council are gratefully acknowledged.

[63] Philippa Browning thanks the reviewers for their assistance in evaluating this paper.

References

Bale, S. D., M. J. Reiner, J. L. Bougeret, M. L. Kaiser, S. Krucker, D. E. Larson, and R. P. Lin (1999), The source region of an interplanetary type II radio burst, *Geophys. Res. Lett.*, *26*, 1573–1576, doi:10.1029/1999GL900293.

Benz, A. O., and T. Golla (1988), Radio emission of coronal shock waves, *Astron. Astrophys.*, *202*, 267–274.

Cairns, I. H. (1986), The source of free energy for type II solar radio bursts, *Proc. Astron. Soc. Aust.*, *6*, 444–446.

Cairns, I. H. (2011), Coherent radio emissions associated with solar system shocks, in *The Sun, the Solar Wind, and the Heliosphere*, edited by M. P. Miralles and J. Almeida, pp. 267–338, Springer, New York.

Cairns, I. H., and S. A. Knock (2006), Predictions for dynamic spectra and source regions of type II radio bursts in the inhomogeneous corona and solar wind, in *Planetary Radio Emissions VI*, edited by H. O. Rucker, W. S. Kurth, and G. Mann, pp. 419–430, Osterr. Akad. Wissenschaften, Vienna.

Cane, H. V., R. G. Stone, J. Fainberg, R. T. Stewart, J. L. Steinberg, and S. Hoang (1981), Radio evidence for shock acceleration of electrons in the solar corona, *Geophys. Res. Lett.*, *8*(12), 1285–1288, doi:10.1029/GL008i012p01285.

Cane, H. V., N. R. Sheeley, and R. A. Howard (1987), Energetic interplanetary shocks, radio emission, and coronal mass ejections, *J. Geophys. Res.*, *92*(A9), 9869–9874, doi:10.1029/JA092iA09p09869.

Cargill, P. J., J. M. Schmidt, D. S. Spicer, and S. T. Zalesak (2000), Magnetic structure of overexpanding coronal mass ejections: Numerical models, *J. Geophys. Res.*, *105*(A4), 7509–7520, doi:10.1029/1999JA900479.

DeVore, C. R. (1991), Flux-corrected transport techniques for multidimensional compressible MHD, *J. Comput. Phys.*, *92*, 142–160.

Dulk, G. A., Y. Leblanc, T. S. Bastian, and J.-L. Bougeret (2000), Acceleration of electrons at type II shock fronts and production of shock-accelerated type III bursts, *J. Geophys. Res.*, *105*(A12), 27,343–27,352, doi:10.1029/2000JA000076.

Florens, M. S. L., I. H. Cairns, S. A. Knock, and P. A. Robinson (2007), Data-driven solar wind model and prediction of type II bursts, *Geophys. Res. Lett.*, *34*, L04104, doi:10.1029/2006GL028522.

Gopalswamy, N. (2006), Coronal mass ejections of solar cycle 23, *J. Air Waste Manage. Assoc.*, *27*, 243–254.

Gopalswamy, N., A. Lara, R. P. Lepping, M. L. Kaiser, D. Berdichevsky, and O. C. St. Cyr (2000), Interplanetary acceleration of coronal mass ejections, *Geophys. Res. Lett.*, *27*(2), 145–148, doi:10.1029/1999GL003639.

Gopalswamy, N., E. Aguilar-Rodriguez, S. Yashiro, S. Nunes, M. L. Kaiser, and R. A. Howard (2005), Type II radio bursts and energetic solar eruptions, *J. Geophys. Res.*, *110*, A12S07, doi:10.1029/2005JA011158.

Gosling, J. T., P. Riley, D. J. McComas, and V. J. Pizzo (1998), Over-expanding coronal mass ejections at high heliographic latitudes: Observations and simulations, *J. Geophys. Res.*, *103*(A2), 1941–1954, doi:10.1029/97JA01304.

Hillan, D., I. H. Cairns, and P. A. Robinson (2012a), Type II solar radio bursts: Modeling and extraction of shock parameters, *J. Geophys. Res.*, *110*, A03104, doi:10.1029/2011JA016754.

Hillan, D., I. H. Cairns, and P. A. Robinson (2012b), Type II solar radio bursts: 2. Detailed comparison of theory with observations, *J. Geophys. Res.*, *117*, A06105, doi:10.1029/2011JA016755.

Hoang, S., C. Lacombe, R. J. MacDowall, and G. Thejappa (2007), Radio tracking of the interplanetary coronal mass ejection driven shock crossed by Ulysses on 10 May 2001, *J. Geophys. Res.*, *112*, A09102, doi:10.1029/2006JA011906.

Holman, G. D., and M. E. Pesses (1983), Solar type II radio emission and the shock drift acceleration of electrons, *Astrophys. J.*, *267*, 837–843.

Hundhausen, A. J. (1999), Coronal mass ejections, in *The Many Faces of the Sun: A Summary of the Results From NASA's Solar Maximum Mission*, edited by K. T. Strong et al., pp. 143–200, Springer, New York.

Knock, S. A., and I. H. Cairns (2005), Type II radio emission predictions: Sources of coronal and interplanetary spectral structure, *J. Geophys. Res.*, *110*, A01101, doi:10.1029/2004JA010452.

Knock, S. A., I. H. Cairns, P. A. Robinson, and Z. Kuncic (2001), Theory of type II radio emission from the foreshock of an interplanetary shock, *J. Geophys. Res.*, *106*(A11), 25,041–25,051, doi:10.1029/2001JA000053.

Knock, S. A., I. H. Cairns, P. A. Robinson, and Z. Kuncic (2003a), Theoretically predicted properties of type II radio emission from an interplanetary foreshock, *J. Geophys. Res.*, *108*(A3), 1126, doi:10.1029/2002JA009508.

Knock, S. A., I. H. Cairns, and P. A. Robinson (2003b), Type II radio emission predictions: Multiple shock ripples and dynamic spectra, *J. Geophys. Res.*, *108*(A10), 1361, doi:10.1029/2003JA009960.

Lengyel-Frey, D., T. Golla, R. J. MacDowall, R. G. Stone, and J. L. Philips (1997), Ulysses observations of wave activity at interplanetary shocks and implications for type II radio bursts, *J. Geophys. Res.*, *102*(A2), 2611–2621,doi:10.1029/96JA02871.

Magdalenić, J., B. Vršnak, and H. Aurass (2002), Solar type II radio bursts: Emission from shock segments with a collapsing trap geometry?, *Eur. Space Agency Spec. Publ.*, *ESA SP-506*, 335–338.

Maia, D., M. Pick, A. Vourlidas, and R. Howard (2000), Development of coronal mass ejections: Radio shock signatures, *Astrophys. J.*, *528*, L49–L51.

Maksimovic, M., V. Pierrard, and P. Riley (1997), Ulysses electron distributions fitted with Kappa functions, *Geophys. Res. Lett.*, *24*(9), 1151–1154, doi:10.1029/97GL00992.

Mann, G., and A. Klassen (2005), Electron beams generated by shock waves in the solar corona, *Astron. Astrophys.*, *441*, 319–326.

Nelson, G. J., and D. B. Melrose (1985), Type II bursts, in *Solar Radiophysics: Studies of Emission From the Sun at Metre Wavelengths*, edited by D. J. McLean and N. R. Labrum, p. 333, Cambridge Univ. Press, New York.

Neugebauer, M., and J. Giacolone (2005), Multispacecraft observations of interplanetary shocks: Nonplanarity and energetic particles, *J. Geophys. Res.*, *110*, A12106, doi:10.1029/2005JA011380.

Nindos, A., C. E. Alissandrakis, A. Hillaris, and P. Preka-Papadema (2011), On the relationship of shock waves to flares and coronal mass ejections, *Astron. Astrophys.*, *531*, A31, doi:10.1051/0004-6361/201116799.

Pilipp, W. G., H. Miggenrieder, K. H. Müllhäuser, H. Rosenbauer, R. Schwenn, and F. M. Neubauer (1987), Variations of electron distribution functions in the solar wind, *J. Geophys. Res.*, *92*(A2), 1103–1118, doi:10.1029/JA092iA02p01103.

Prestage, N. (1994), Compendium of significant solar radiospectrograph events from June 1992 to June 1994, *IPS Radio Space Serv. Tech. Rep. TR-94-01*, 85 pp., Aust. Gov. Dep. of Admin. Serv., West Chatswood, N. S. W., Australia.

Pulupa, M. P., S. D. Bale, and J. C. Kasper (2010), Langmuir waves upstream of interplanetary shocks: Dependence on shock and plasma parameters, *J. Geophys. Res.*, *115*, A04106, doi:10.1029/2009JA014680.

Reiner, M. J., and M. L. Kaiser (1999), High-frequency type II radio emissions associated with shocks driven by coronal mass ejections, *J. Geophys. Res.*, *104*(A8), 16,979–16,991, doi:10.1029/1999JA900143.

Reiner, M. J., M. L. Kaiser, J. Fainberg, J. L. Bougeret, and R. G. Stone (1997), Remote radio tracking of interplanetary CMEs, in *Correlated Phenomena at the Sun in the Heliosphere and in Geospace*, *ESA SP-415*, edited by B. Fleck, pp. 183–188, Eur. Space Agency, Noordwijk, Netherlands.

Reiner, M. J., M. L. Kaiser, J. Fainberg, and R. G. Stone (1998), A new method for studying remote type II radio emissions from coronal mass ejection-driven shocks, *J. Geophys. Res.*, *103*(A12), 29,651–29,664, doi:10.1029/98JA02614.

Robinson, P. A., and I. H. Cairns (1998a), Fundamental and harmonic emission in type III solar radio bursts. Part I: Emission at a single location or frequency, *Sol. Phys.*, *181*, 363–394.

Robinson, P. A., and I. H. Cairns (1998b), Fundamental and harmonic emission in type III solar radio bursts. Part II: Dominant modes and dynamic spectra, *Sol. Phys.*, *181*, 395–428.

Schmidt, J. M., and I. H. Cairns (2012), Type II radio bursts: 1. New entirely analytic formalism for the electron beams, Langmuir waves, and radio emission, *J. Geophys. Res.*, *117*, A04106, doi:10.1029/2011JA017318.

Schmidt, J. M., and P. J. Cargill (2003), Magnetic reconnection between a magnetic cloud and the solar wind magnetic field, *J. Geophys. Res.*, *108*(A1), 1023, doi:10.1029/2002JA009325.

Schmidt, J. M., and N. Gopalswamy (2008), Synthetic radio maps of CME-driven shocks below 4 solar radii heliocentric distance, *J. Geophys. Res.*, *113*, A08104, doi:10.1029/2007JA013002.

Smerd, S. F., K. V. Sheridan, and R. T. Stewart (1974), On split-band structure in type II radio bursts from the Sun, in *Coronal Disturbances: Proceedings of the IAU Symposium 57*, edited by G. Newkirk, p. 389–393, Reidel, Dordrecht, Netherlands.

St. Cyr, O. C., et al. (2000), Properties of coronal mass ejections: SOHO LASCO observations from January 1996 to June 1998, *J. Geophys. Res.*, *105*(A8), 18,169–18,186, doi:10.1029/1999JA000381.

Stewart, R. T., and A. Magun (1980), Radio evidence for electron acceleration by transverse shock waves in herringbone Type II solar bursts, *Proc. Astron. Soc. Aust.*, *4*(1), 53–55.

Temmer, M., B. Vršnak, T. Žic, and A. M. Veronig (2009), Analytic modeling of the Moreton wave kinematics, *Astrophys. J.*, *702*, 1343–1352.

Vršnak, B., H. Aurass, J. Magdalenić, and N. Gopalswamy (2001), Band-splitting of coronal and interplanetary type II bursts. I. Basic properties, *Astron. Astrophys.*, *377*, 321–329.

Wild, J. P., and S. F. Smerd (1972), Radio bursts from the solar corona, *Annu. Rev. Astron. Astrophys.*, *10*, 159–196.

Zalesak, S. T. (1979), Fully multidimensional flux-corrected transport algorithms for fluids, *J. Comput. Phys.*, *31*, 335–362.